

Article

A First-Principles Study of Nonlinear Elastic Behavior and Anisotropic Electronic Properties of Two-Dimensional HfS₂

Mahdi Faghinasiri¹, Aidin Ahmadi¹, Samaneh Alvankar Golpayegan²,
Saeideh Garosi Sharifabadi² and Ali Ramazani^{3,*} 

¹ Computational Materials Science Laboratory, Nano Research and Training Center, Tehran 19967-15433, Iran; mahdi.faghinasiri@gmail.com (M.F.); aidin.ahmadiiii@gmail.com (A.A.)

² Department of Physics, K.N. Toosi University of Technology, Tehran 19967-15433, Iran; sama.alvankr@gmail.com (S.A.G.); sgarosi@mail.kntu.ac.ir (S.G.S.)

³ Department of Mechanical Engineering, Massachusetts Institute of Technology, 77 Massachusetts Ave., Cambridge, 02139 MA, USA

* Correspondence: ramazani@mit.edu

Received: 29 January 2020; Accepted: 26 February 2020; Published: 1 March 2020



Abstract: We utilize first principles calculations to investigate the mechanical properties and strain-dependent electronic band structure of the hexagonal phase of two dimensional (2D) HfS₂. We apply three different deformation modes within −10% to 30% range of two uniaxial (D1, D2) and one biaxial (D3) strains along *x*, *y*, and *x-y* directions, respectively. The harmonic regions are identified in each deformation mode. The ultimate stress for D1, D2, and D3 deformations is obtained as 0.037, 0.038 and 0.044 (eV/Ång³), respectively. Additionally, the ultimate strain for D1, D2, and D3 deformation is obtained as 17.2, 17.51, and 21.17 (eV/Ång³), respectively. In the next step, we determine the second-, third-, and fourth-order elastic constants and the electronic properties of both unstrained and strained HfS₂ monolayers are investigated. Our findings reveal that the unstrained HfS₂ monolayer is a semiconductor with an indirect bandgap of 1.12 eV. We then tune the bandgap of HfS₂ with strain engineering. Our findings reveal how to tune and control the electronic properties of HfS₂ monolayer with strain engineering, and make it a potential candidate for a wide range of applications including photovoltaics, electronics and optoelectronics.

Keywords: HfS₂; density functional theory; mechanical properties; bandgap; elastic constants

1. Introduction

The rise of two-dimensional (2D) materials began in 2004 with a focus on graphene sheets by Novoselov and Geim [1]. Graphene is a 2D layer of sp²-bonded carbons as the first prototype of 2D layered materials, which is viewed as an ideal material for a wide range of applications including photonics, THz electronics, nonlinear optics, sensors, and transparent electrodes [2–5]. 2D materials have been intensively researched for the next generation of ultrathin and flexible electronic and optoelectronic devices, including transistors, phototransistors, solar cells, and light-emitting diodes (LEDs) [6–9]. These materials have historically been one of the most extensively studied classes of materials due to their wealth of significant physical phenomena, which can occur when charge and heat transports are confined to a 2D surface [10–12].

Recently, atomically thin 2D materials, such as graphene, hexagonal boron nitride (*h*-BN), and the transition-metal dichalcogenides (TMDs) have received a lot of interests due to their unique electronic and optoelectronic properties. The TMDs with a general formula of MX₂ (M = transition metal, X = S, Se, Te) are particularly an interesting class of 2D materials comprising both metallic and

semiconducting behaviors [10]. Semiconducting TMDs have advantages over gapless graphene in their application for logic transistors since their sizable bandgap is necessary to achieve high on/off ratio [12]. Among TMDs, MoS₂ is the most widely investigated as a semiconducting TMD. MoS₂-based transistors have shown an extremely high room-temperature current on/off ratio of ≈ 108 and mobility of higher than 200 cm²/(V s), which is comparable to the mobility achieved in thin silicon films [13] and graphene nanoribbons [14–17]. Other members in the TMD family are still in the stage of exploration. For example, group IVB (Hf and Zr)-based TMDs are theoretically predicted to have higher mobility (mobility of HfS₂ = 1833 cm²/(V s), HfSe₂ = 3579 cm²/(V s), ZrS₂ = 1247 cm²/(V s), ZrSe₂ = 2316 cm²/(V s)) and higher sheet current density than group VIB (Mo and W)-based TMDs [6,18,19]. In contrast to graphene with zero bandgap, TMD-VIB monolayers possess sizable electrical performance [3,4,20,21] and optoelectronic properties [6,22,23]. For instance, the HfS₂ monolayer is semiconductor with an indirect bandgap of about 2eV, according to the experimental measurements [18,19,24,25].

In addition, ultrathin HfS₂ not only shows faster and higher response, but also higher stability in comparison to most of the other 2D materials, which makes HfS₂ an appropriate positional candidate for the electronic and optoelectronic applications [7,26].

The HfS₂ monolayer shows isotropic elastic parameters (i.e. in-plane stiffness and Poisson's ratio), which are the same as those for MoS₂ in both armchair and zigzag directions. When the strain along both x and y directions increases, the bandgap of HfS₂ increases, while the bandgap of MoS₂ decreases. Therefore, the same as MoS₂, the band structure of HfS₂ can also be effectively tuned by applying uniaxial strains [27].

In the current research, we first employ density functional theory (DFT) to study the mechanical properties (strain-stress energy), and elastic constants under different deformation modes. Then, we do strain engineering to tune the electronic properties of the HfS₂ monolayer and make it a potential candidate for different applications.

2. Computational Details

We performed DFT calculations with the Quantum ESPRESSO package [28,29] using projector-augmented wave (PAW) method. We used the Perdew–Burke–Ernzerhof exchange–correlation functional, revised for solids (PBEsol) along with the projector-augmented wave (PAW) potentials for the selfconsistent total energy calculations and geometry optimization [30]. Eighteen valence electrons of Hf atoms (4f¹⁴ 5d² 6s²) and six valence electrons of S atoms (3s² 4p⁴) were included in the computations. For the plane-wave expansion, the cutoff energy after convergence is set to 880 eV. The Brillouin zone sampled using a 20 × 20 × 1 Monkhorst–Pack *k*-point grid [31]. Atomic positions were relaxed until the energy differences are converged within 10^{−6} eV and the maximum Hellmann–Feynman force on any atom is below 10^{−6} eV. A vacuum of 15 Å along the *c* direction was included to safely avoid the interaction between the periodically repeated structures. Under various deformation tensors, the total energy of the system is calculated and led to achieve energy-strain curves. Here, the strained energy per atom is defined as below:

$$E_S = \frac{E_{tot} - E_0}{n} \quad (1)$$

Where E_{tot} , and E_0 are the total energy of the strained and unstrained HfS₂ monolayers, respectively. n is also the number of atoms in the unit cell. The DFT simulation calculates the true or Cauchy stresses, σ , which for the HfS₂ monolayer should be expressed as a 2D force per length with the unit of N/m by taking the product of the Cauchy stresses (with the unit of N/m²) and the super-cell thickness of 15 Å. The Cauchy stresses are related to the second Piola–Kirchhoff (PK2) stresses Σ as [32]:

$$\Sigma = JF^{-1}\sigma(F^{-1})^T \quad (2)$$

where, F is the deformation gradient tensor [32], J is the determinant of F , and σ is the true stress with the unit of N/m. In continuum theory of elasticity [32], and finite element method [33], the second *P*-*K* stress is employed to explore the impact of large forces on the mechanical behavior of materials [34].

Polynomial fitting of the resultant second P - K strain-stress curves on the DFT results has been conducted to calculate the second-, third-, and fourth-order elastic constants using continuum theory of elasticity.

To identify the elastic constants, the obtained strain-stress curves from DFT calculations are fitted to the constitutive equations of the continuum theory of elasticity. The second-order elastic constants (C_{11} , C_{12} , C_{22} , and C_{66}) are the representative of the linear elastic response of the structure, while the higher-order (third-, and fourth-s order) constants are essential to the study of nonlinear elastic behavior of materials, as Wei et al. [35], Peng et al. [32], and Faghihnasiri et al. [6–9] described it completely for Boron nitride, graphene, and borophene monolayers, respectively. To identify the elastic constants, suitable deformations should be selected to facilitate the calculation of these constants directly from the stress-strain curves. For this purpose, three different types of deformations modes (strain tensors (D_1 , D_2 , and D_3)) is this study, which are previously defined by Wei et al. [35], Peng et al. [32], and Faghihnasiri et al. [9].

Additionally, using the second-order elastic constants, bulk modulus (K), shear modulus (G), Young's modulus (Y) and Poisson's ratio (ν) can calculated in x and y directions. We utilize the following formulas for 2D materials to calculate these parameters [36,37]:

$$\gamma_x^{2D} = \frac{(C_{11}C_{22} - C_{12}^2)}{C_{11}}, \quad \gamma_y^{2D} = \frac{(C_{11}C_{22} - C_{12}^2)}{C_{22}} \quad (3)$$

$$\nu_x^{2D} = C_{12}/C_{11}, \quad \nu_y^{2D} = C_{12}/C_{22} \quad (4)$$

$$G^{2D} = C_{66} \quad (5)$$

$$K_{x,y} = \frac{\gamma_{x,y}^{2D}}{2(1 - \nu_{x,y}^{2D})} \quad (6)$$

3. Results and Discussion

3.1. Atomic Structure

HfS₂ monolayer is in a hexagonal phase with an inversion center at the Hf atom sites. Each Hf atom is bounded to six S atoms. The unit cell consists of one Hf atom, and two S atoms. The geometric structure of a HfS₂ monolayer is depicted in Figure 1. The obtained optimized lattice constant of HfS₂ is 3.64 Å, which is in good agreement with the lattice constant of bulk HfS₂, which is reported as 3.63 Å using PBE based calculations [38], and 3.61 Å utilizing vdW-TS/HI method [39]. As can be seen in Table 1, the optimized lattice constant of HfS₂ is in a geed agreement with reported lattice constant of similar 2D materials including HfSe₂, ZrS₂, ZrSe₂, GaS, GaSe, and InSe in the literature. The bond length between Hf and S atoms is also calculated as 2.55 Å (Figure 1b). This value is in good agreement with reported data in the literature (2.59 Å) [40]. The bond angle between Hf and S atoms (atoms No. 1, 2, and 3) is 88.80°.

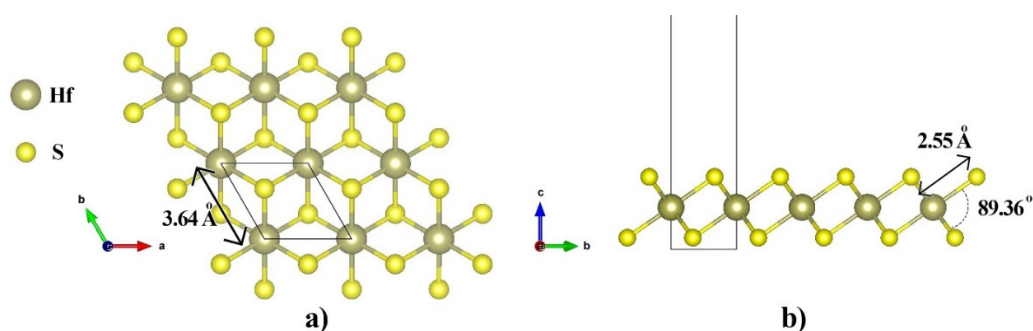


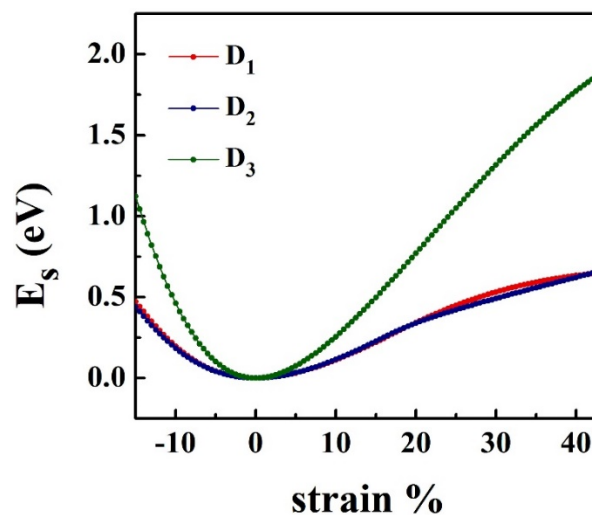
Figure 1. (a) Top view and (b) side view of the atomic structure of the hexagonal HfS₂ monolayer. The light brown and yellow balls represent Hf and S atoms, respectively. The black rectangle denotes the unit cell.

Table 1. Comparison of the lattice constants of 2D HfS₂ are calculated using different exchange-correlation functions along with the other reported values in the literature.

Material	Method	Lattice Constant
HfS ₂	PBEsol (This work)	3.64
	GGA [40]	3.54
	HSE [40]	3.53
	LDA [40]	3.38
	PBE (bulk) [41]	3.54
	PBE (bulk) [38]	3.63
	vdW-TS/HI [39]	3.61
HfSe ₂	vdW-TS/HI [39]	3.70
ZrS ₂	vdW-TS/HI [39]	3.64
ZrSe ₂	vdW-TS/HI [39]	3.74
GaS	DFT-PBE [41]	3.64
GaSe	DFT-PBE [41]	3.82
InSe	DFT-PBE [41]	4.09

3.2. Mechanical Properties

The energy-strain curves for HfS₂ monolayer under three types of deformations, namely uniaxial strain along x (D_1), y (D_2) and biaxial strain along x - y (D_3), is analyzed and demonstrated in Figure 2. It is evident that E_s differs from the applied strain along with x and y directions. For the tensile and compressive strains through all three modes, E_s becomes asymmetric. The strained energy is a quadratic function of strain in the range between $-3\% \leq \eta \leq 5\%$ for the uniaxial strain along x direction. For the uniaxial strain along y direction and biaxial strain, these harmonic region ranges between $-7\% \leq \eta \leq 3\%$ and $-2\% \leq \eta \leq 2\%$, respectively.

**Figure 2.** The energy-strain per atom of HfS₂ monolayer under the uniaxial strain along x (D_1) and y (D_2) directions, and biaxial strain along x - y (D_3).

In all three deformation modes, the total energy of the system increases with increasing the applying strain. As can be seen in Figure 2, The changes of E_s with strain for D_1 and D_2 deformation modes is almost the same. However, for D_3 deformation mode, the rate of energy change with strain is much higher (Figure 2).

3.3. Strain-Stress Relationship

Figure 3 shows the strain-stress relations obtained from the DFT calculations as well as the fits to these by the equations of continuum theory of elasticity. As can be seen in this figure, the stress-strain curves are depicted for all D_1 , D_2 , and D_3 deformation modes.

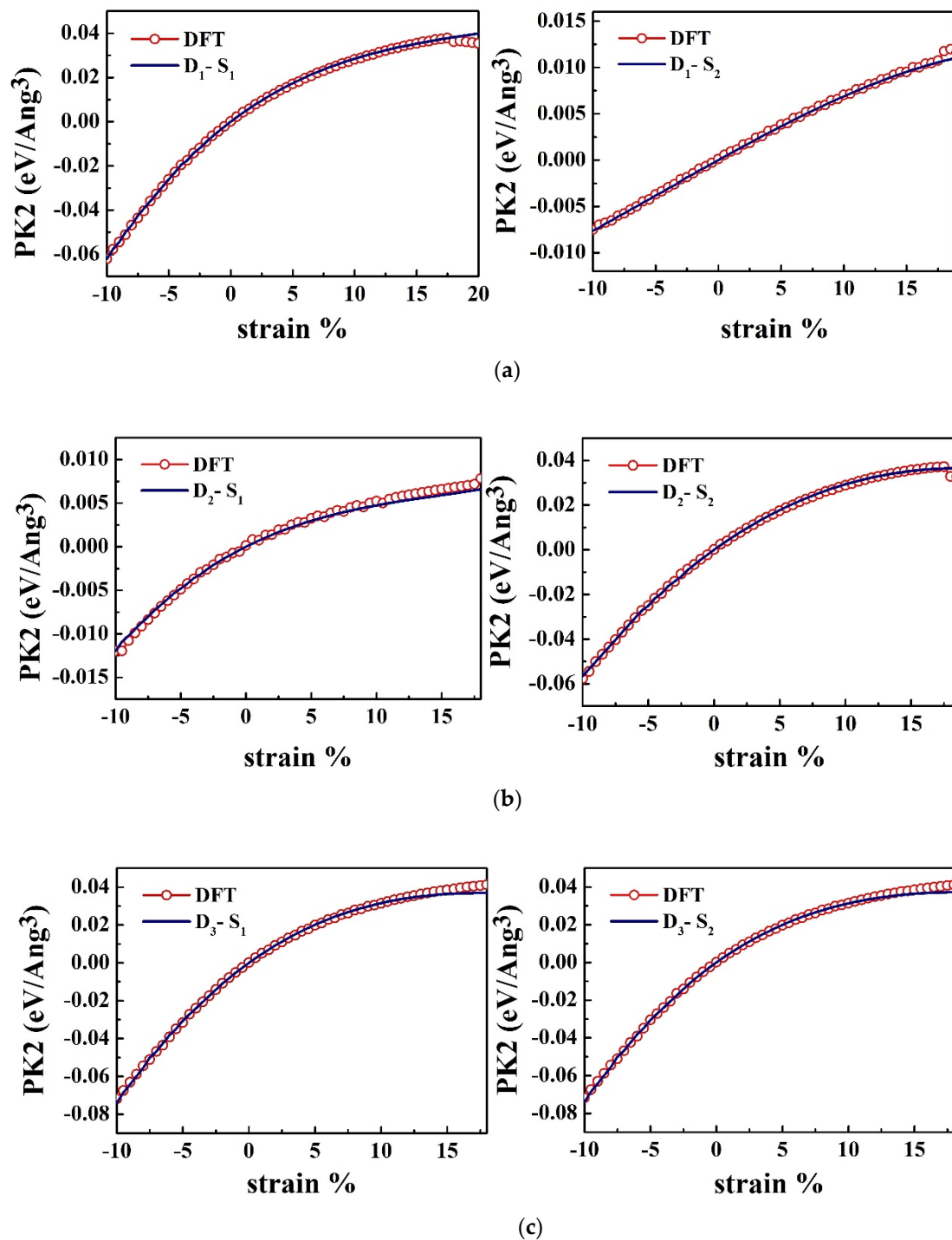


Figure 3. Strain-stress relationships for three types of strain, namely (a) D_1 (b) D_2 (c) D_3 , fitted with S_1 and S_2 , which denote to the x and y components of the stress, respectively.

The maximum value in the stress-strain curves shows the ultimate tensile strength (Σ_m) of the material, in which a material can suffer the maximum respective η_m without damaging (Figure 4).

The ultimate strain reflects the intrinsic bonding strengths and acts as a lower limit of the critical strain. Additionally, the values obtained for the ultimate stress and ultimate strain is given in Table 2. Beyond the ultimate strain, the materials will get in a metastable state, which ends up with fracture [42]. The DFT results for strains below the ultimate strain are used to determine the higher-order elastic constants.

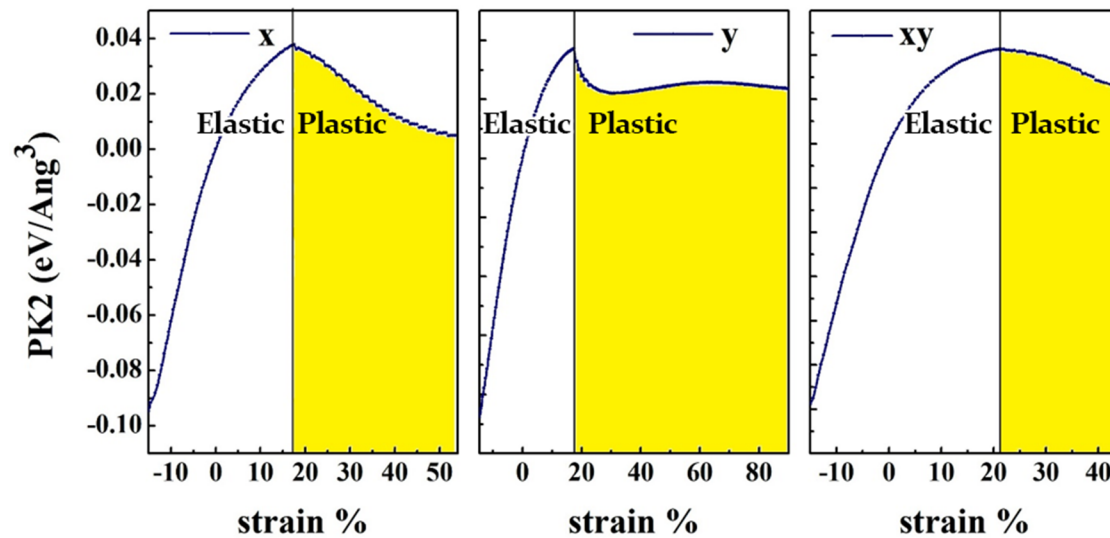


Figure 4. Σ_m and η_m denote the x , y , and x - y components of the stress and strain, respectively. The line separates the harmonic and anharmonic regions. The yellow area shows the plastic region.

Table 2. Ultimate strains (η_m) and ultimate stresses (Σ_m) for three (D_1 , D_2 , and D_3) types of strains.

	Uniaxial (x)	Uniaxial (y)	Biaxial (x - y)
Σ_m (eV/Å ³)	0.037	0.038	0.044
η_m	17.2%	17.51%	21.17%

As can be seen in Figure 4, the stress increases linearly with increasing strain, within the harmonic (elastic) region. Under larger strains, for the prediction of strain-stress curves, the system is in the anharmonic region in which higher-order terms must be perceived as well. As mentioned previously, the system transits from elastic to the plastic region, when exposed to higher strains. Eventually, Table 3 prepares the nonzero second-, third- and fourth- order elastic constants (SOEC, TOEC and FOEC, respectively) for the HfS₂ monolayer.

Table 3. Nonzero second-, third- and fourth-order elastic constants (in N/m) for the HfS₂ monolayer.

SOEC		TOEC		FOEC	
C_{11}	86.29	C_{111}	−683.81	C_{1111}	3389.08
C_{12}	15.28	C_{112}	−14.69	C_{1112}	−343.81
C_{22}	85.71	C_{222}	−561.10	C_{2222}	1092.89
C_{66}	68.14	C_{122}	−145.42	C_{1222}	968.49
		C_{166}	−205.85	C_{6666}	−592.82
		C_{266}	−1118	C_{1266}	2386.80
				C_{1122}	−42.83
				C_{2266}	−2207.16
				C_{1166}	471.75

To comprehensively understand the magnitudes of elastic constants obtained in this work for HfS₂, Table 4 presents multiple comparisons between our findings and the other reported elastic constants

for similar structures. Furthermore, 2D Young's moduli (in-plane stiffness) along x and y directions (Y_x^{2D} , Y_y^{2D}), Poisson's ratio along x and y directions (ν_x^{2D} , ν_y^{2D}), 2D shear modulus (G^{2D}), and the 2D bulk modulus (K), are tabulated in Table 5 and validated by those reported for other structurally similar compounds in the literature.

Table 4. Elastic constants C_{11} and C_{12} obtained in this work along with those reported in a previous works (in units of N/m).

Material	C_{11}	C_{12}
HfS ₂ (This work)	86.29	15.28
GaS [41]	83	18
GaSe [41]	70	16
InSe [41]	51	12
h-BN [32]	293.2	66.1
ZrS ₂ [39]	131.47	25.63
ZrSe ₂ [39]	104.62	21.31
HfS ₂ [39]	141.98	25.95
HfSe ₂ [39]	116.88	22.30

Ref [39] is in the bulk structure.

Table 5. 2D Young's moduli, Poisson's ratio, 2D shear modulus, and 2D bulk modulus for some 2D materials.

Material	Y_x^{2D} (N/m)	Y_y^{2D} (N/m)	ν_x^{2D}	ν_y^{2D}	G^{2D} (N/m)	K (N/m)
HfS ₂	83.01	83.57	0.17	0.17	68.14	50.85
ZrS ₂ [39]		57.22		0.20	23.85 (GPa)	31.73 (GPa)
ZrSe ₂ [39]		52.33		0.19	22.02 (GPa)	27.99 (GPa)
HfSe ₂ [39]		69.59		0.19	29.34 (GPa)	36.87 (GPa)
h-BN [32]		279.2		0.2176	-	160 (GPa)

3.4. Electronic Properties

First, we studied the electronic properties of HfS₂ in the absence of strain. Figure 5 shows the band structure of the strained structure of HfS₂, which is obtained from PBEsol calculations. As can be seen in Figure 5, HfS₂ is a semiconductor with an indirect bandgap of 1.12 eV. This value is compared with other methods of HfS₂ ($E_g^{LDA} = 1.07$ eV [40], $E_g^{GGA} = 1.15$ eV [43], $E_g^{HSE06} = 2.02$ eV [44], and $E_g^{GW} = 2.45$ eV [45]), where it is in a good agreement with $E_g^{GGA} = 1.15$ eV [43]. As can be seen in Table 4, The predicted gap energies by GW and HSE06 are larger than the predicted gap energy by PBE approximation. Since the HSE06 functional can accurately predict enthalpies of formation, ionization potentials, and electron affinities for lattice constants and band gaps of solids in general, the predicted gap energy by HSE06 is larger and more accurate than the predicted gap energy by PBE [46]. Also, in GW calculations, the excitonic effects are included and due to the fact that the excitonic effects are significant in 2D semiconductors, the predicted gap energy by GW is twice larger than the predicted gap energy by GGA approximation for the HfS₂ monolayer (Table 4) [47].

In our predicted electronic structure (Figure 5), it can be seen that the conduction-band minimum (CBM) and valence-band maximum (VBM) are located at M and Γ points, respectively. Additionally, we examine the projected density of states (PDOS), which demonstrates the contribution of orbitals in the valence and conduction bands of the material. In the conduction band, Hf-5d orbitals have the maximum contribution. In contrast, the 3p orbital of S atom makes a greater contribution in the valence band near the Fermi level, as shown in Figure 5b.

In the next step, we investigated the electronic behavior of HfS₂ under different strains. The bandgap variation of HfS₂ monolayer under these three types of strain are shown in Figure 6a. as can be seen in this figure, for all deformation modes, the bandgap decreases when the compressive strain increases 0% to 10%, while it increases when the tensile strain increases from 0% to 10%. In this

strain range, we note that the rate of the gap energy decrease/increase with strain is almost the same for D1 and D2 deformation modes. From 10% to 16% tensile strain, the energy gap decreases for all deformation modes. For the strain range from 16% to 20%, the energy gap increases by increasing strain for D1 and D2 deformations, while it keeps decreasing for D3. For the tensile strain ranging from 20% to 30%, the gap energy is almost constant with strain for D1 and D2, while it keeps decreasing for D3. At 22%, 24%, 28% strains along x direction (D_1), and at 12%, 14%, 16%, 20%, 22% strains along y direction (D_2), the bandgap becomes direct. Under biaxial strain (D_3), the semiconducting monolayer maintains its indirect nature, while its energy gap increases with increasing strain and reaches its maximum value (1.79 eV) at 10% strain. For the uniaxial strain in both D_1 and D_2 cases, when the compressive strain increases from zero to 2%, the energy gap decreases and then gradually increases by increasing the amount of the compressive strain from 2% to 5%. Then, by increasing the strain from 5% to 10%, the energy gap reduces again. For D3 case, the energy gap decreases by increasing the compressive strain from 0 to 10% deformation. As can be seen in Figure 6a, the material becomes metal ($E_g = 0$ eV) at 10% compressive strain in all three deformation modes. The value of energy gap is the same (1.6 eV) for D_1 and D_3 at 18% strain, and for D_2 at 17.5% strain. As can be observed in Figure 4, at 18% D_1 and 17.5% D_2 types of deformation, the material is in plastic region, while at 18% D_3 type deformation, the material shows elastic deformation (Figure 6b,c,d). As can be seen in Figure 6d, the elastic to plastic transition for D3 occurs at 22% strain.

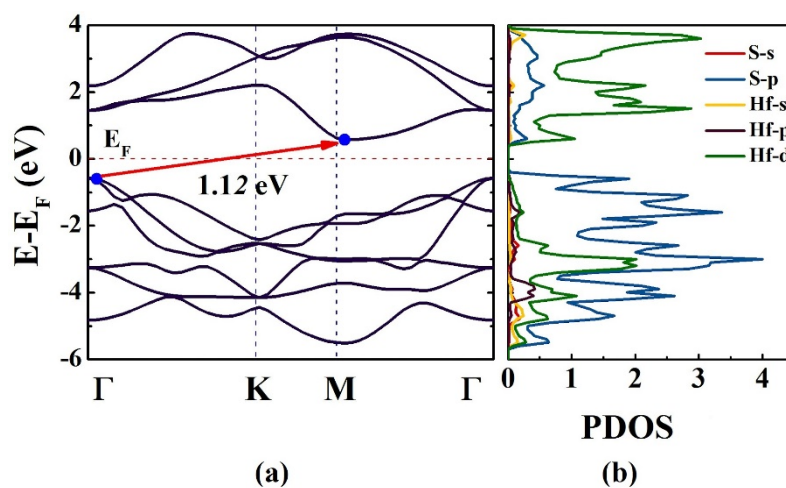


Figure 5. Band structure (a) and PDOS (b) of the HfS_2 monolayer in free-strain condition. The Fermi level is set to zero.

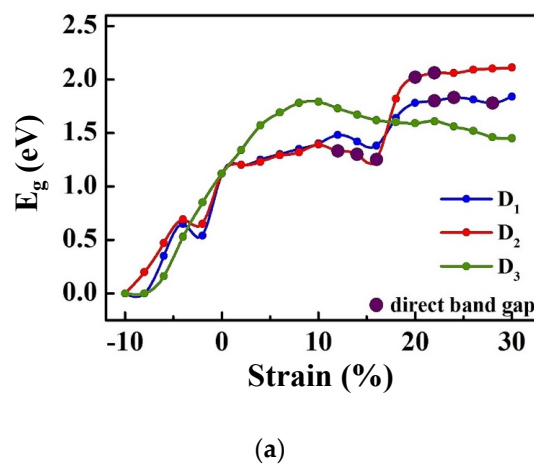


Figure 6. Cont.

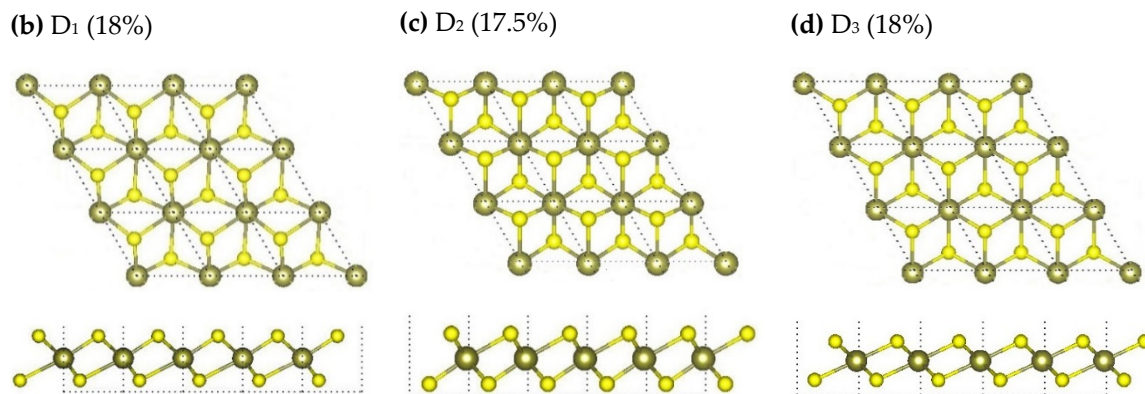


Figure 6. (a) The bandgap variations of the HfS₂ monolayer under uniaxial strain along x (D_1) and y (D_2) directions and the biaxial strains along x - y (D_3). (b) The deformed lattice structures of the HfS₂ monolayer at uniaxial 18% tensile strain along x direction (D_1), (c) the deformed lattice structures of the HfS₂ monolayer at under uniaxial strains of 17.5% along y direction, and (d) the deformed lattice structures of the HfS₂ monolayer at 18% biaxial strain along x - y directions (D_3). The top and side views are shown in the top and bottom panels, respectively.

Our findings indicate that the electronic properties of HfS₂ can be effectively tuned by applying planar forces to HfS₂ in different directions. Figure 7 shows the band structures of the HfS₂ monolayer under uniaxial compressive and tensile strains along the x direction (D_1) within the range of -10% to 30% . As can be seen in Figure 7, when the strain ranges from -10% to -8% , bands of energies cross the Fermi level so that HfS₂ at these strains under D_1 deformation shows a metallic behavior. By reducing the value of strain to -6% , the HfS₂ monolayer becomes an indirect semiconductor with a bandgap of 0.35 eV. At the strains above 22% , the bandgap becomes direct and energy of bandgap increases up to 1.8 eV for the D_1 case.

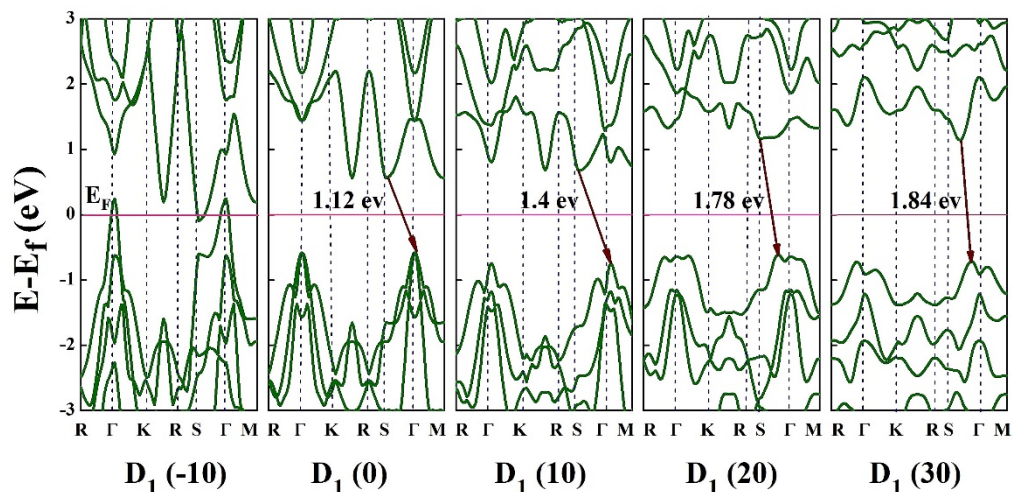


Figure 7. Band structure of HfS₂ monolayer under the uniaxial strains in the range of -10% to 30% along x direction. The Fermi level is set to zero.

In Figure 7, the conduction-band minimum (CBM) is located at S point, while the valence-band maximum (VBM) is located at the Γ point, which is shifted to the S point by increasing the strain. These points indicate the transformation of bandgap from indirect to direct with strain engineering.

For the deformed HfS₂ under the tensile strain along y direction (D_2), by increasing the strains from 0% to 30% , the bandgap increases from 1.12 eV to its maximum value of 2.11 eV continuously. The band structure of strain HfS₂ monolayer under uniaxial compressive and tensile strain along y direction (D_2) is shown in Figure 8. Under the compressive strain of D_2 deformation, there is

no bandgap near the Fermi level so the system is metallic. In addition, it remains as an indirect semiconductor over the entire applied compressive strain domain when it is strained along y direction (D_2). However, under tensile straining, at 12% to 22% strains, the gap is direct and energy bandgap changes from 1.33 to 2.06 eV. When the compressive strain is applied (D_2), the located CBM at S point moves to Γ point, and the VBM at the Γ point moves to M point. By applying tensile strain, CBM gets away from the Fermi level and the bandgap increases from 1.12 eV (at unstrained condition) to 2.11 eV (strained with 30% tensile strain).

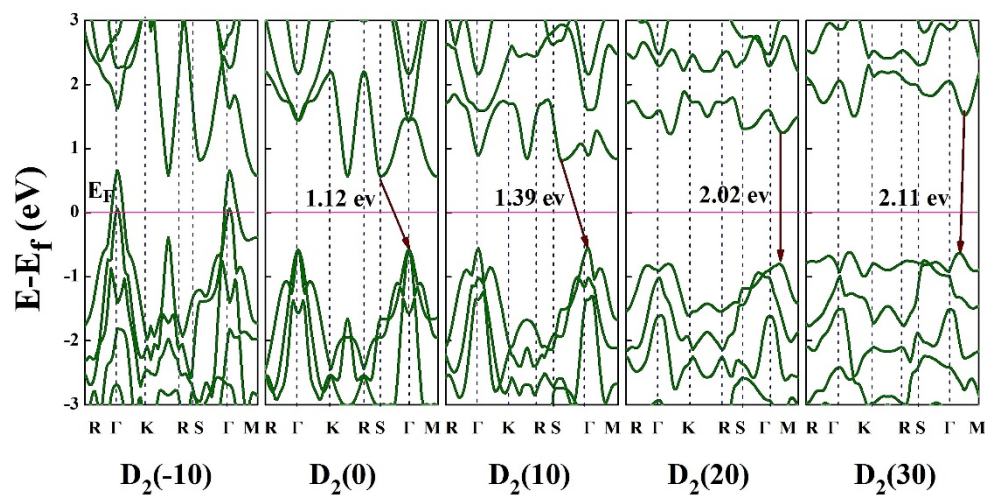


Figure 8. Electronic band structure of HfS_2 monolayer under the uniaxial strains in the range of -10% to 30% along y direction. The Fermi level is set to zero.

In Figure 9 the band structure of strained HfS_2 monolayer under biaxial strain along x - y (D_3) ranging from -10% to 30% strain is shown. As can be seen in Figure 9, under compressive strain ranging from -10% to -6% strains, the bands cross the Fermi level and the system shows metallic behavior. At -6% strain and beyond ($-6 < \text{strain} < 0$), the HfS_2 monolayer becomes an indirect semiconductor with a bandgap of 0.16 eV in -6% strain. In the tensile deformation domain, the gap energy increases increasing the strain. At 0% , 10% , 20% , and 30% strains, the bandgap becomes 1.12 eV, 1.79 eV, 1.59 eV and 1.45 eV, respectively. The CBM is located at M , Γ , Γ and K point for 0% , 10% , 20% , and 30% strain, respectively. Also, the VBM at 0% , 10% , 20% strains are located between M and Γ points and at 30% strain, it is located between Γ and K points.

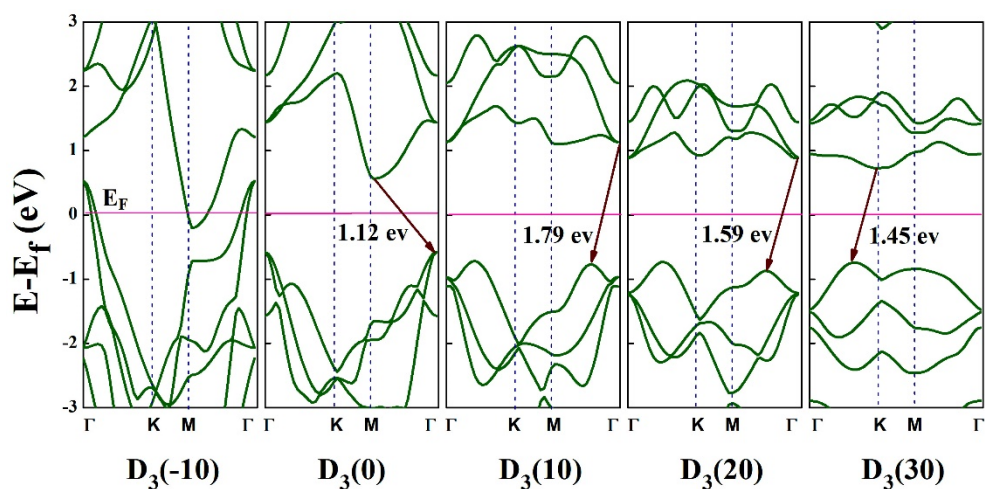


Figure 9. Band structure of the HfS_2 monolayer under D_3 deformation in the range of -10% to 30% .

Graphene has a plate structure and its symmetry is not broken during deformation. Therefore, not only graphene does not suffer any bulking during deformation, but also only monotonic changes can occur on its electron properties during the biaxial straining (Figure 10) [48]. While, the HfS₂ structure is not a plate like structure, its electronic properties are affected by the occurred buckling during the deformation. It is expected to observe many changes in the symmetry of the structure and the distance and angle of the atoms in the strained HfS₂ monolayers. Such structural changes can greatly affect the electronic properties and therefore, the bandgap changes of HfS₂ will not be monotonic under biaxial strains (Figure 6).

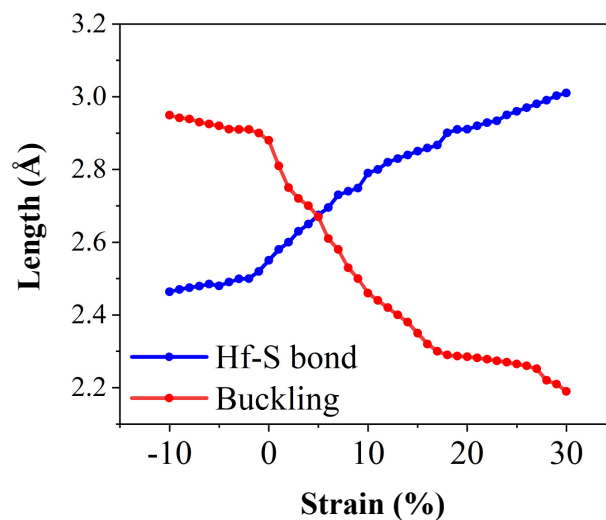


Figure 10. Hf-S bond length and buckling of the HfS₂ monolayer under D₃ deformation in the range of −10% to 30% straining.

4. Conclusions

In summary, the mechanical and electronic properties of the HfS₂ monolayer under two uniaxial (D₁ and D₂) and one biaxial (D₃) DFT calculations is investigated. We determined the harmonic regions in the different deformation modes. This harmonic region ranges in $-3\% \leq \eta \leq 5\%$, $-7\% \leq \eta \leq 3\%$ and $-2\% \leq \eta \leq 2\%$ for D₁, D₂, and D₃, respectively. Our findings reveal that the ultimate stress of the HfS₂ monolayer for D₁, D₂, and D₃ is $0.037 \frac{eV}{\text{Å}^3}$, $0.038 \frac{eV}{\text{Å}^3}$, and $0.044 \frac{eV}{\text{Å}^3}$, respectively. The obtained ultimate strain is 17%, 17.5% and 21% strain for D₁, D₂, and D₃ respectively. The high order of elastic constants including second-, third-, and fourth-order constants are calculated. The values of 2D Young's moduli along *x* and *y* directions are predicted as 83.01 N/m and 83.57 N/m, respectively. The value of Poisson's ratio along *x* and *y* directions is the same (0.17) for both D1 and D2.

Moreover, the electronic properties of HfS₂ show that it is a semiconductor with an indirect bandgap of 1.12 eV. The projected density of states (PDOS) indicates the conduction band, Hf-5d orbital possesses the maximum contribution, while the 3p orbital of S atom have greatest contribution in the valance band. The variation of band structure and bandgap of the HfS₂ monolayer under D₁, D₂, and D₃ deformation modes in the range of −10% to 30% are also investigated. We tuned the bandgap state (direct vs. indirect), gap energy (opening vs. shrinking), and phase transition (semiconductor-metal) by strain engineering under different deformation modes. Our findings reveal how to utilize strain engineering to make HfS₂ monolayer as a suitable candidate for a wide range of applications including flexible solar cells, electronics and optoelectronics.

Author Contributions: DFT calculations: M.F., S.A.G., S.G.S., and A.A.; validation: M.F., and A.A.; analysis M.F., and A.A.; writing—original draft preparation: M.F., and A.A.; writing—review and editing: A.R.; and supervision: A.R. All authors have read and agreed to the published version of the manuscript.

Funding: This research received no external funding.

Conflicts of Interest: The authors declare no competing financial interest.

References

1. Kang, J.; Tongay, S.; Zhou, J.; Li, J.; Wu, J. Band offsets and heterostructures of two-dimensional semiconductors. *Appl. Phys. Lett.* **2013**, *102*, 012111. [[CrossRef](#)]
2. Neto, A.; Novoselov, K. Two-dimensional crystals: Beyond graphene. *Mater. Express* **2011**, *1*, 10–17. [[CrossRef](#)]
3. Gui, G.; Li, J.; Zhong, J. Band structure engineering of graphene by strain: First-principles calculations. *Phys. Rev. B* **2008**, *78*, 075435. [[CrossRef](#)]
4. Chhowalla, M.; Shin, H.S.; Eda, G.; Li, L.-J.; Loh, K.P.; Zhang, H. The chemistry of two-dimensional layered transition metal dichalcogenide nanosheets. *Nat. Chem.* **2013**, *5*, 263. [[CrossRef](#)]
5. Ansari, R.; Malakpour, S.; Faghihnasiri, M.; Ajori, S. Structural and elastic properties of carbon nanotubes containing Fe atoms using first principles. *Superlattices Microstruct.* **2013**, *64*, 220–226. [[CrossRef](#)]
6. Butler, S.Z.; Hollen, S.M.; Cao, L.; Cui, Y.; Gupta, J.A.; Gutiérrez, H.R.; Heinz, T.F.; Hong, S.S.; Huang, J.; Ismach, A.F.; et al. Progress, challenges, and opportunities in two-dimensional materials beyond graphene. *ACS Nano* **2013**, *7*, 2898–2926. [[CrossRef](#)]
7. Xu, K.; Wang, Z.; Wang, F.; Huang, Y.; Wang, F.; Yin, L.; Jiang, C.; He, J. Ultrasensitive Phototransistors Based on Few-Layered HfS₂. *Adv. Mater.* **2015**, *27*, 7881–7887. [[CrossRef](#)]
8. Ahmadi, A.; Faghihnasiri, M.; Shiraz, H.G.; Sabeti, M. Mechanical properties of graphene and its analogous decorated with Na and Pt. *Superlattice Microstruct.* **2017**, *101*, 602–608. [[CrossRef](#)]
9. Faghihnasiri, M.; Jafari, H.; Ramazani, A.; Shabani, M.; Estalaki, S.M.; Larson, R.G. Nonlinear elastic behavior and anisotropic electronic properties of two-dimensional borophene. *J. Appl. Phys.* **2019**, *125*, 145107. [[CrossRef](#)]
10. Wang, Q.H.; Kalantar-Zadeh, K.; Kis, A.; Coleman, J.N.; Strano, M.S. Electronics and optoelectronics of two-dimensional transition metal dichalcogenides. *Nat. Nanotechnol.* **2012**, *7*, 699. [[CrossRef](#)]
11. Abderrahmane, A.; Ko, P.; Thu, T.; Ishizawa, S.; Takamura, T.; Sandhu, A. High photosensitivity few-layered MoSe₂ back-gated field-effect phototransistors. *Nanotechnology* **2014**, *25*, 365202. [[CrossRef](#)] [[PubMed](#)]
12. Liu, W.; Kang, J.; Sarkar, D.; Khatami, Y.; Jena, D.; Banerjee, K. Role of metal contacts in designing high-performance monolayer n-type WSe₂ field effect transistors. *Nano Lett.* **2013**, *13*, 1983–1990. [[CrossRef](#)] [[PubMed](#)]
13. Gomez, L.; Aberg, I.; Hoyt, J. Electron transport in strained-silicon directly on insulator ultrathin-body n-MOSFETs with body thickness ranging from 2 to 25 nm. *IEEE Electron Device Lett.* **2007**, *28*, 285–287. [[CrossRef](#)]
14. Derived, C. Ultrasmooth Graphene Nanoribbon Semiconductors. *Science* **2008**, *319*, 1229–1232.
15. Zhang, W.; Huang, Z.; Zhang, W.; Li, Y. Two-dimensional semiconductors with possible high room temperature mobility. *Nano Res.* **2014**, *7*, 1731–1737. [[CrossRef](#)]
16. Zhao, X.; Wang, T.; Wang, G.; Dai, X.; Xia, C.; Yang, L. Electronic and magnetic properties of 1T-HfS₂ by doping transition-metal atoms. *Appl. Surf. Sci.* **2016**, *383*, 151–158. [[CrossRef](#)]
17. Ahmadi, A.; Jafari, H.; Rajipour, M.; Fattahi, R.; Faghihnasiri, M. Nonlinear electronic transport behavior of γ -graphyne nanotubes. *IEEE Trans. Electron Devices* **2019**, *66*, 1584–1590. [[CrossRef](#)]
18. Novoselov, K.S.; Jiang, D.; Schedin, F.; Booth, T.J.; Khotkevich, V.V.; Morozov, S.V.; Geim, A.K. Two-dimensional atomic crystals. *Proc. Natl. Acad. Sci. USA* **2005**, *102*, 10451–10453. [[CrossRef](#)]
19. Novoselov, K.S.; Geim, A.K.; Morozov, S.V.; Jiang, D.; Zhang, Y.; Dubonos, S.V.; Grigorieva, I.V.; Firsov, A.A. Electric field effect in atomically thin carbon films. *Science* **2004**, *306*, 666–669. [[CrossRef](#)]
20. Krowne, C.M. Introduction to examination of 2D hexagonal band structure from a nanoscale perspective for use in electronic transport devices. *Adv. Imag. Elect. Phys.* **2019**, *210*, 1.
21. Krowne, C.M. Graphyne and Borophene as Nanoscopic Materials for Electronics. *arXiv* **2019**, arXiv:1912.10876.
22. Schwierz, F. Graphene transistors. *Nat. Nanotechnol.* **2010**, *5*, 487. [[CrossRef](#)] [[PubMed](#)]
23. Hu, P.; Wen, Z.; Wang, L.; Tan, P.; Xiao, K. Synthesis of few-layer GaSe nanosheets for high performance photodetectors. *ACS Nano* **2012**, *6*, 5988–5994. [[CrossRef](#)] [[PubMed](#)]
24. Radisavljevic, B.; Radenovic, A.; Brivio, J.; Giacometti, I.V.; Kis, A. Single-layer MoS₂ transistors. *Nat. Nanotechnol.* **2011**, *6*, 147. [[CrossRef](#)] [[PubMed](#)]
25. Chen, H.; Müller, M.B.; Gilmore, K.J.; Wallace, G.G.; Li, D. Mechanically strong, electrically conductive, and biocompatible graphene paper. *Adv. Mater.* **2008**, *20*, 3557–3561. [[CrossRef](#)]

26. Chen, J. Phonons in bulk and monolayer HfS₂ and possibility of phonon-mediated superconductivity: A first-principles study. *Solid State Commun.* **2016**, *237*, 14–18. [[CrossRef](#)]
27. Kang, J.; Sahin, H.; Peeters, F.M. Mechanical properties of monolayer sulphides: A comparative study between MoS₂, HfS₂ and TiS₃. *Phys. Chem. Chem. Phys.* **2015**, *17*, 27742–27749. [[CrossRef](#)]
28. Blöchl, P.E. Projector augmented-wave method. *Phys. Rev. B* **1994**, *50*, 17953. [[CrossRef](#)]
29. Espresso, Q. A modular and open-source software project for quantum simulations of materials/P. *J. Phys. Condens. Matter* **2009**, *21*, 395502.
30. Perdew, J.P.; Ruzsinszky, A.; Csonka, G.; Vydrov, O.A.; Scuseria, G.E.; Constantin, L.A.; Zhou, X.; Burke, K. Restoring the density-gradient expansion for exchange in solids and surfaces. *Phys. Rev. Lett.* **2008**, *100*, 136406. [[CrossRef](#)]
31. Monkhorst, H.J.; Pack, J.D. Special points for Brillouin-zone integrations. *Phys. Rev. B* **1976**, *13*, 5188. [[CrossRef](#)]
32. Peng, Q.; Ji, W.; De, S. Mechanical properties of the hexagonal boron nitride monolayer: Ab initio study. *Comput. Mater. Sci.* **2012**, *56*, 11–17. [[CrossRef](#)]
33. Reddy, J.N. *An Introduction to the Finite Element Method*, 3rd ed.; McGraw Hill: New York, NY, USA, 2006.
34. Hammerand, D.C.; Kapania, R.K. Thermoviscoelastic analysis of composite structures using a triangular flat shell element. *AIAA J.* **1999**, *37*, 238–247. [[CrossRef](#)]
35. Wei, X.; Fregneaud, B.; Marianetti, C.A.; Kysar, J.W. Nonlinear elastic behavior of graphene: Ab initio calculations to continuum description. *Phys. Rev. B* **2009**, *80*, 205407. [[CrossRef](#)]
36. Thorpe, M.; Sen, P. Elastic moduli of two-dimensional composite continua with elliptical inclusions. *J. Acoust. Soc. Am.* **1985**, *77*, 1674–1680. [[CrossRef](#)]
37. Andrew, R.C.; Mapasha, R.E.; Ukpong, A.M.; Chetty, N. Mechanical properties of graphene and boronitrene. *Phys. Rev. B* **2012**, *85*, 125428. [[CrossRef](#)]
38. Lv, H.; Lu, W.; Luo, X.; Lu, H.; Zhu, X.; Sun, Y. Enhancing the thermoelectric performance of a HfS₂ monolayer through valley engineering. *arXiv* **2016**, arXiv:1608.05464.
39. Zhao, Q.; Guo, Y.; Si, K.; Ren, Z.; Bai, J.; Xu, X. Elastic, electronic, and dielectric properties of bulk and monolayer ZrS₂, ZrSe₂, HfS₂, HfSe₂ from van der Waals density-functional theory. *Phys. Status Solidi* **2017**, *254*, 1700033. [[CrossRef](#)]
40. Singh, D.; Gupta, S.K.; Sonvane, Y.; Kumar, A.; Ahuja, R. 2D-HfS₂ as an efficient photocatalyst for water splitting. *Catal. Sci. Technol.* **2016**, *6*, 6605–6614. [[CrossRef](#)]
41. Rasmussen, F.A.; Thygesen, K.S. Computational 2D materials database: Electronic structure of transition-metal dichalcogenides and oxides. *J. Phys. Chem. C* **2015**, *119*, 13169–13183. [[CrossRef](#)]
42. Topsakal, M.; Cahangirov, S.; Ciraci, S. The response of mechanical and electronic properties of graphene to the elastic strain. *Appl. Phys. Lett.* **2010**, *96*, 091912. [[CrossRef](#)]
43. Ahuja, R.; Piquini, P.C. HfS₂ and TiS₂ Monolayers with Adsorbed C, N, P Atoms: A First Principles Study. *Catalysts* **2020**, *10*, 2073–4344.
44. Lu, H.; Guo, Y.; Robertson, J. Band edge states, intrinsic defects, and dopants in monolayer HfS₂ and SnS₂. *Appl. Phys. Lett.* **2018**, *112*, 062105. [[CrossRef](#)]
45. Zhuang, H.L.; Hennig, R.G. Computational search for single-layer transition-metal dichalcogenide photocatalysts. *J. Phys. Chem. C* **2013**, *117*, 20440–20445. [[CrossRef](#)]
46. Krukau, A.V.; Vydrov, O.A.; Izmaylov, A.F.; Scuseria, G.E. Influence of the exchange screening parameter on the performance of screened hybrid functionals. *J. Chem. Phys.* **2006**, *125*, 224106. [[CrossRef](#)]
47. Ugeda, M.M.; Bradley, A.J.; Shi, S.F.; Felipe, H.; Zhang, Y.; Qiu, D.Y.; Ruan, W.; Mo, S.K.; Hussain, Z.; Shen, Z.X.; et al. Crommie. Giant bandgap renormalization and excitonic effects in a monolayer transition metal dichalcogenide semiconductor. *Nat. Mater.* **2014**, *13*, 1091–1095. [[CrossRef](#)]
48. Katin, K.P.; Krylov, K.S.; Maslov, M.M.; Mur, V.D. Tuning the supercritical effective charge in gapless graphene via Fermi velocity modifying through the mechanical stretching. *Diam. Relat. Mater.* **2019**, *100*, 107566. [[CrossRef](#)]

